J. Fluid Mech. (1997), *vol.* 349, *pp.* 95–115. Printed in the United Kingdom

Two-dimensional shock tube flow for dense gases

By B. P. BROWN AND B. M. ARGROW

Department of Aerospace Engineering Sciences, University of Colorado, Boulder, CO 80309, USA

(Received 17 February 1996 and in revised form 23 May 1997)

Non-stationary oblique shock wave reflections for fluids in the dense gas regime are examined for selected cases. A time-accurate predictor-corrector TVD scheme with reflective boundary conditions for solving the Euler equations simulates the evolution of a wave field for an inviscid van der Waals gas near the thermodynamic critical point. The simulated cases involve shock tube flows with compressive wedges and circular arcs. Non-classical phenomena, such as disintegrating shocks, expansion shocks, composite waves, etc., demonstrate significant differences from perfect gas flow fields over similar geometries. Detailed displays of wave field structures and thermodynamic states for the dense gas flow fields are presented and analysed.

1. Introduction

Heavy polyatomic gases with large specific heats may exhibit non-classical fluid dynamic phenomena near the thermodynamic critical point. There is increased interest in these gases since their unusual properties could prove to be advantageous in several engineering applications. For example, the application of dense gases in nozzles and heavy-gas wind tunnels has been investigated by Aldo & Argrow (1995), Anders (1993), Kluwick (1993), Schnerr & Leidner (1993*a*), and Anderson (1991). Working fluids used in organic Rankine cycles (Curran 1981) may potentially exhibit advantageous dense gas effects. A recent discussion of using dense gases in turbomachinery can be found in Schnerr & Leidner (1993*b*).

In the following discussion, *dense gas* refers to a single-phase fluid whose heat capacity is large enough to potentially exhibit non-classical phenomena in the thermodynamic state above the saturated vapour curve near the thermodynamic critical point. The phrase *dense gas regime* refers to the aforementioned thermodynamic region and *dense gas flow* indicates all or part of a flow field with thermodynamic states in the dense gas regime. Bethe (1942) and Zel'dovich (1946) were the first to suggest the existence of dense gases by demonstrating thermodynamic regions of what is referred to as *negative non-linearity*. Thompson (1971) was the first to recognize the importance of the sign of a fluid parameter that governs the nonlinear dynamics of gases called the *fundamental derivative of gas dynamics*,

$$\Gamma = -\frac{\overline{v}}{2}\frac{\left(\partial^2\overline{p}/\partial\overline{v}^2\right)_{\overline{s}}}{\left(\partial\overline{p}/\partial\overline{v}\right)_{\overline{s}}} = 1 + \frac{\overline{\rho}}{\overline{a}}\left(\frac{\partial\overline{a}}{\partial\overline{\rho}}\right)_{\overline{s}}. \tag{1.1}$$

Here, $\overline{p}$ is the pressure, $\overline{\rho}$ is the density, $\overline{v} = 1/\overline{\rho}$ is the specific volume, $\overline{a}$ is the speed of sound, $\overline{s}$ is the entropy, and the overbar indicates dimensional quantities. The fundamental derivative Γ describes the rate of change of the convected sound

speed with density for a simple wave as indicated by the second formulation in (1.1). In the perfect gas regime, $\Gamma > 0$ and the gas dynamics is said to exhibit positive non-linearity. Negative nonlinearity occurs in the thermodynamic region where $\Gamma < 0$ and the curvature of the isentropes is reversed near the saturation curve in the vicinity of the critical point. Note that the term $(\partial^2 \overline{p}/\partial \overline{v}^2)$ in (1.1) is negative between the inflection points of the isentropes. This results in $\Gamma < 0$ since the denominator $(\partial \overline{p}/\partial \overline{v})_{\overline{s}} < 0$ everywhere from the requirement of thermodynamic stability. An example of an isentrope inflection and the corresponding $\Gamma < 0$ region is evident in the p, v diagram in figure 5(d). One result of the $\Gamma < 0$ condition is that flow disturbances can only steepen backwards to form expansion shocks. This is in contrast to classical flows where disturbances steepen forward to form compression shocks. For fluids with relatively small specific heats, such as steam, a $\Gamma < 0$ region does not exist above the saturation curve for the van der Waals model. Owing to the contributions of the three investigators mentioned above, fluids with specific heats large enough to exhibit a region of negative non-linearity above the saturation curve are sometimes referred to as Bethe–Zel'dovich–Thompson (BZT) fluids (Cramer 1991*a*).

Using several gas models Lambrakis & Thompson (1972) and Thompson & Lambrakis (1973) analytically show specific examples of existing fluids such as fluorinated ether E-4 ($C_{14}F_{29}HO_4$) and perfluorodecalin ($C_{10}F_{18}$) where negative non-linearity may be observed. Cramer (1989*a*) confirms these findings and extends the list of negative-Γ fluids to several other commercially available fluorocarbons. Borisov *et al.* (1983) experimentally observed what they believed to be expansion shocks in trifluorochloromethane ($CClF_3$, Freon-13), although this has since been questioned (Cramer & Sen 1986). Thompson, Carofano & Kim (1986) also experimentally observed non-classical flow phenomena including expansion shocks in multi-phase flows.

In Cramer & Best (1991) as well as Schnerr & Leidner (1991) are examples of additional analytical investigation of the inviscid structure of dense gas flows. The dissipative structure of weak shocks in the dense gas regime is also analytically examined by Cramer & Kluwick (1984) and Cramer (1987). Numerical simulation of the evolution of dense gas wave fields is performed by Thompson *et al.* (1986) for multi-phase fluids and Argrow (1996) for single-phase one-dimensional shock tube flow. The work presented in the present article is an extension of the latter research to a two-dimensional shock tube with obstacles. Owing to the complexity of the state equations for dense gases, wave interactions are expected to be less predictable than the interactions in perfect gas flows.

There have been extensive investigations of shock wave reflections over the past several decades for perfect gases, equilibrium gases, and non-equilibrium gases. A comprehensive source list and an encompassing survey of research in this area can be found in Ben-Dor (1992). Of particular relevance to our work are the findings for moving shocks incident on compressive wedges. For perfect gases, the wave field structures are found to be solely dependent on the Mach number of the incident shock M_I and the angle of the wedge θ_w for a given ratio of specific heats γ. Figure 1(a), a reproduction of figure 2.41 from Ben-Dor (1992), is a θ_w, M_I diagram for frozen argon (note M_I is labelled M_S in this figure). The four types of reflections observed experimentally generally agree with the analytically determined domains and transition boundaries. Low incident wave Mach numbers ($M_I < 2$) at low wedge angles ($\theta_w < 50^\circ$) usually result in a single Mach reflection (SMR) while high wedge angles ($\theta_w > 50^\circ$) result in a regular reflection (RR). These wave structures are illustrated in figure 1(b) and figure 1(c), respectively. For higher incident wave Mach

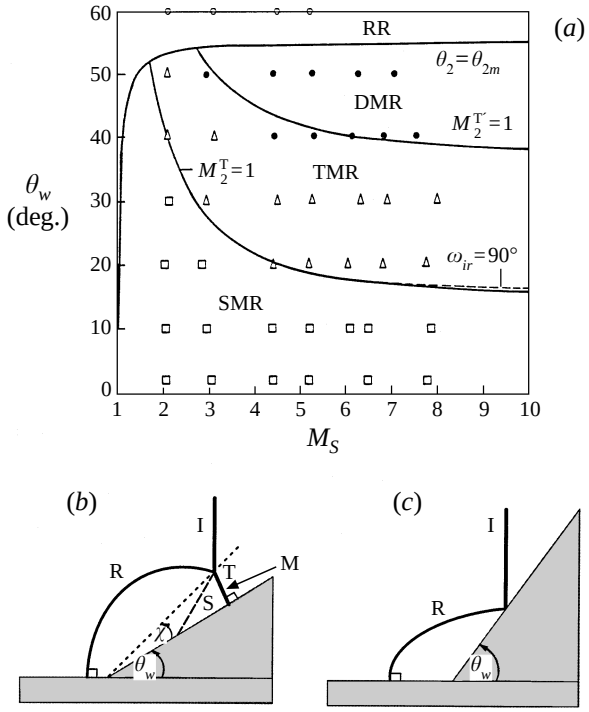

FIGURE 1. Shock reflections in argon. (*a*) A reproduction of figure 2.41 from Ben-Dor (1992): domains and transition boundaries for various types of shock wave reflections in the (M_I, θ_w) plane for frozen argon; lines are the analytically determined transition lines and the symbols are the experimental data. (*b*) A single Mach reflection (SMR); I, incident shock wave; R, reflected shock wave; M, Mach stem; S, slipstream; T, triple point; θ_w, wedge angle; χ, triple-point trajectory angle. (*c*) A regular reflection (RR).

numbers ($M_I > 2$), a transitional Mach reflection (TMR) or a double Mach reflection (DMR) will be observed. Incident shock wave speeds in the dense gas regime are generally very low ($M_I \leqslant 1.23$ for the cases presented here). Thus, wave field structures in the dense gas regime are more likely to be similar to a SMR or a RR.

Shock wave reflections in the dense gas regime can differ from those of a perfect gas since the fundamental derivative Γ may be negative in some regions of the flow. Thompson (1971) shows that for steady flows compression shocks disintegrate into finite compression waves when $\Gamma < 0$. This is also true for compression shocks in unsteady flows. Because the region of negative nonlinearity is restricted to a finite range of temperatures and pressures, waves interacting with other waves or boundaries may cause Γ to change sign. The result of the interaction could be non-classical wave phenomena. Cramer (1989*b*) demonstrates conditions where a compression wave can appear as a composite wave, e.g. a shock–fan combination, or even a split wave, e.g. a shock–fan–shock combination. Argrow (1996) shows that waves reflected from shock tube endwalls may become composite, split, or completely reversed in nature, i.e. shocks reflecting as fans or vice versa, depending on the sign of Γ both upstream and through the wave.

This paper provides the first detailed computational analysis of single-phase dense gas wave fields for two-dimensional shock tube flow with obstacles. A predictor-corrector TVD scheme (Causon 1988) based on the Davis–Roe flux-limited method

(Davis 1987) is used to numerically integrate the time-dependent two-dimensional Euler equations for a van der Waals gas. The wave field simulations include compression shocks incident on wedges of varying angles as well as circular arcs. Expansion shocks incident on wedges are also simulated. The purpose of this paper is to demonstrate through the simulation and analysis of the selected cases some of the non-classical phenomena that will occur. A comprehensive analysis of all reflection types and transition criteria for dense gas wave structures will be the focus of future research.

2. Governing equations

2.1. *Gas model*

The thermal equation of state is that of a van der Waals gas,

$$\overline{p} = \frac{\overline{\rho}\overline{R}\overline{T}}{1 - \overline{b}\overline{\rho}} - \overline{\alpha}\overline{\rho}^2, \tag{2.1}$$

where $\overline{p}$ is the pressure, $\overline{R}$ is the gas constant, $\overline{T}$ is the temperature, and $\overline{\alpha}$ and $\overline{b}$ are the well-known van der Waals constants. The caloric state equation is written as

$$\overline{e} = \overline{e}_0 + \overline{c}_v \overline{T} - \overline{\alpha}\overline{\rho}, \tag{2.2}$$

where $\overline{e}$ is the specific internal energy and $\overline{e}_0$ is a reference value. For simplicity, the specific heat $\overline{c}_v$ is assumed to be a constant evaluated in the perfect gas limit since there is minimal temperature change in the flows investigated. The thermodynamic variables are non-dimensionalized using the critical point values, designated with a c subscript,

$$\left.\begin{aligned} p = \frac{\overline{p}}{\overline{p}_c}, \quad \rho = \frac{\overline{\rho}}{\overline{\rho}_c}, \quad T = \frac{\overline{T}}{\overline{T}_c}, \quad u = \frac{\overline{u}}{(\overline{R}\overline{T}_c)^{1/2}}, \quad v = \frac{\overline{v}}{(\overline{R}\overline{T}_c)^{1/2}}, \\ e = \frac{\overline{e} - \overline{e}_c}{\overline{R}\overline{T}_c}, \quad s = \frac{\overline{s} - \overline{s}_c}{\overline{R}}, \quad a = \frac{\overline{a}}{(\overline{R}\overline{T}_c)^{1/2}}, \quad x = \frac{\overline{x}}{\overline{L}}, \quad y = \frac{\overline{y}}{\overline{L}}. \end{aligned}\right\} \tag{2.3}$$

The variables x and y are the non-dimensional streamwise and transverse spatial coordinates, respectively, and $\overline{L}$ is the length of the computational domain. The variables u and v are the velocity components in the streamwise and transverse directions, respectively.

Equations (2.1) and (2.2) are written in reduced variable form by setting the compressibility factor at the critical point, $Z_c = (\overline{p}/\overline{\rho}\overline{R}\overline{T})_c = 3/8$:

$$p = \frac{8\rho T}{3 - \rho} - 3\rho^2, \tag{2.4}$$

$$e = \frac{T}{\delta} - \frac{9}{8}\rho. \tag{2.5}$$

Note that the free parameters $\overline{\alpha}$ and $\overline{b}$ have been eliminated. This, of course, indicates that all fluids satisfy the same state equation when reduced variables are used which satisfies the *principle of corresponding states* (e.g. Emanuel 1987). The parameter $\delta = \overline{R}/\overline{c}_v$ is assumed to be constant. Air with a specific heat ratio of $\gamma = 1.4$ has a value of $\delta = 0.4$. For the dense gas cases a value of $\delta = 0.0125$ is used, corresponding to a fluid with large specific heat relative to the gas constant $\overline{R}$. For example, commercially available fluids such as perfluorodecane ($C_{10}F_{22}$) has $\delta = 0.0132$ and

fluorinated ether E-5 ($C_{17}F_{35}HO_5$) has $\delta = 0.0074$ (Thompson & Lambrakis 1973). The non-dimensional form of other useful properties can also be derived:

$$a = \left[(1+\delta)T\left(\frac{3}{3-\rho}\right)^2 - \frac{9}{4}\rho\right]^{1/2}, \tag{2.6}$$

$$s = \ln\left[\frac{1}{2}\left(\frac{3-\rho}{\rho}\right)\right] + \frac{1}{\delta}\ln T, \tag{2.7}$$

$$\Gamma = \frac{6}{\delta a_r{}^2}\left[\left(\frac{1}{3-\rho}\right)^3(2+3\delta+\delta^2)T - \frac{\rho}{4}\right]. \tag{2.8}$$

In equation (2.8) a_r is the reduced speed of sound given by

$$a_r{}^2 = \frac{1}{\delta}\left[4(1+\delta)T\left(\frac{1}{3-\rho}\right)^2 - \rho\right]. \tag{2.9}$$

2.2. *Euler equations*

The two-dimensional Euler equations,

$$\frac{\partial \boldsymbol{Q}}{\partial t} + \frac{\partial \boldsymbol{E}}{\partial x} + \frac{\partial \boldsymbol{F}}{\partial y} = 0, \tag{2.10}$$

govern the compressible inviscid flow, where the time $t = (\bar{R}\bar{T}_c)^{1/2}\bar{t}/\bar{L}$. The conservative state vector $\boldsymbol{Q}$ and the Cartesian flux vectors $\boldsymbol{E}$ and $\boldsymbol{F}$ have been non-dimensionalized using the relations in (2.3):

$$\boldsymbol{Q} = [\rho,\ \rho u,\ \rho v,\ \rho e_t]^T, \tag{2.11}$$

$$\boldsymbol{E} = \left[\rho u,\ \rho u^2 + Z_c p,\ \rho v u,\ (\rho e_t + Z_c p)u\right]^T, \tag{2.12}$$

$$\boldsymbol{F} = \left[\rho v,\ \rho u v,\ \rho v^2 + Z_c p,\ (\rho e_t + Z_c p)v\right]^T. \tag{2.13}$$

Here, e_t is the specific total energy,

$$e_t = e + \tfrac{1}{2}\left(u^2 + v^2\right). \tag{2.14}$$

3. Numerical method

The physical space (x, y) is mapped onto the computational space (ξ, η) using a generalized coordinate transformation where $\xi = \xi(x, y)$ and $\eta = \eta(x, y)$. The equations of motion become

$$\frac{\partial \hat{\boldsymbol{Q}}}{\partial t} + \frac{\partial \hat{\boldsymbol{E}}}{\partial \xi} + \frac{\partial \hat{\boldsymbol{F}}}{\partial \eta} = 0, \tag{3.1}$$

where

$$\hat{\boldsymbol{Q}} = \boldsymbol{Q}/J, \tag{3.2}$$

$$\hat{\boldsymbol{E}} = \left[\xi_x \boldsymbol{E} + \xi_y \boldsymbol{F}\right]/J, \tag{3.3}$$

$$\hat{\boldsymbol{F}} = \left[\eta_x \boldsymbol{E} + \eta_y \boldsymbol{F}\right]/J. \tag{3.4}$$

Here, $J = \xi_x \eta_y - \xi_y \eta_x$, is the metric Jacobian. The coordinate transformation used to map the H-grid configuration of the shock tube domain into the rectilinear computational domain is

$$\xi = x, \quad \eta = \left[\frac{y - y_l}{1 - y_l}\right]^{\epsilon}, \tag{3.5}$$

where $y_l = y_l(x)$ describes the shape of the lower boundary and ϵ determines the degree of grid clustering at the lower boundary.

A conservative predictor-corrector TVD scheme (PCTVD) is used to solve the non-linear hyperbolic system in (3.1). This pseudo-finite volume method, which is second-order accurate in time and space, is well suited to computing the evolution of shock tube wave fields. Dropping the carets ($\hat{}$) from equations (3.1)–(3.4) for convenience, the formulation of the finite difference equations is written as

$$\boldsymbol{Q}^*_{i,j} = \boldsymbol{Q}^n_{i,j} - \frac{\Delta t}{\Delta \xi}\left(\boldsymbol{E}^n_{i,j} - \boldsymbol{E}^n_{i-1,j}\right) - \frac{\Delta t}{\Delta \eta}\left(\boldsymbol{F}^n_{i,j+1} - \boldsymbol{F}^n_{i,j}\right), \tag{3.6}$$

$$\boldsymbol{Q}^{n+1}_{i,j} = \frac{1}{2}\left[\boldsymbol{Q}^n_{i,j} + \boldsymbol{Q}^*_{i,j} - \frac{\Delta t}{\Delta \xi}\left(\boldsymbol{E}^*_{i,j} - \boldsymbol{E}^*_{i-1,j}\right) - \frac{\Delta t}{\Delta \eta}\left(\boldsymbol{F}^*_{i,j+1} - \boldsymbol{F}^*_{i,j}\right)\right]. \tag{3.7}$$

The asterisk indicates quantities associated with the predictor stage, i and j refer to the spatial discretizations in the ξ- and η-directions, respectively, and n refers to the temporal discretization. The corrector in (3.7) can be brought into TVD form by adding a non-linear term, $\boldsymbol{\Omega}$, that enforces the positivity nonlinear stability condition, reducing significant overshoot at each grid point,

$$\boldsymbol{Q}^{n+1'}_{i,j} = \boldsymbol{Q}^{n+1}_{i,j} + \boldsymbol{\Omega}^n_{i,j}, \tag{3.8}$$

where

$$\begin{aligned}\boldsymbol{\Omega}^n_{i,j} = {} & \left[\boldsymbol{G}^+_{i,j} + \boldsymbol{G}^-_{i+1,j}\right]\Delta\boldsymbol{Q}^n_{i+1/2,j} - \left[\boldsymbol{G}^+_{i-1,j} + \boldsymbol{G}^-_{i,j}\right]\Delta\boldsymbol{Q}^n_{i-1/2,j} \\ & + \left[\boldsymbol{H}^+_{i,j} + \boldsymbol{H}^-_{i,j+1}\right]\Delta\boldsymbol{Q}^n_{i,j+1/2} - \left[\boldsymbol{H}^+_{i,j-1} + \boldsymbol{H}^-_{i,j}\right]\Delta\boldsymbol{Q}^n_{i,j-1/2},\end{aligned} \tag{3.9}$$

$$\boldsymbol{G}^{\pm} = \tfrac{1}{2}\boldsymbol{C}(\zeta)\left[1 - \phi(\boldsymbol{r}^{\pm}_{i,j})\right], \quad \boldsymbol{H}^{\pm} = \tfrac{1}{2}\boldsymbol{C}(\mu)\left[1 - \phi(\boldsymbol{w}^{\pm}_{i,j})\right], \tag{3.10}$$

$$\boldsymbol{C}(z) = \begin{cases} z(1-z), & z \leqslant \frac{1}{2} \\ \frac{1}{4}, & z > \frac{1}{2} \end{cases}, \tag{3.11}$$

$$\phi(z) = \begin{cases} \min\,(2z, 1), & z > 0 \\ 0, & z < 0 \end{cases}, \tag{3.12}$$

$$\boldsymbol{r}^{\pm} = \frac{\left[\Delta\boldsymbol{Q}^n_{i-\frac{1}{2},j},\ \Delta\boldsymbol{Q}^n_{i+\frac{1}{2},j}\right]}{\left[\Delta\boldsymbol{Q}^n_{i\pm\frac{1}{2},j},\ \Delta\boldsymbol{Q}^n_{i\pm\frac{1}{2},j}\right]}, \quad \boldsymbol{w}^{\pm} = \frac{\left[\Delta\boldsymbol{Q}^n_{i,j-\frac{1}{2}},\ \Delta\boldsymbol{Q}^n_{i,j+\frac{1}{2}}\right]}{\left[\Delta\boldsymbol{Q}^n_{i,j\pm\frac{1}{2}},\ \Delta\boldsymbol{Q}^n_{i,j\pm\frac{1}{2}}\right]}, \tag{3.13}$$

$$\zeta = \max\,|\lambda_\xi|\frac{\Delta t}{\Delta \xi}, \quad \mu = \max\,|\lambda_\eta|\frac{\Delta t}{\Delta \eta}. \tag{3.14}$$

Here, [.,.] indicates an inner product, and λ_ξ and λ_η are the eigenvalues in the ξ- and η-directions, respectively. These characteristic values are written as

$$\lambda_\xi = \xi_x u + \xi_y v \pm a(\xi_x^2 + \xi_y^2)^{1/2}, \quad \lambda_\eta = \eta_x u + \eta_y v \pm a(\eta_x^2 + \eta_y^2)^{1/2}. \tag{3.15}$$

Case	δ	ρ_2	p_2	u_2	Γ_2	ρ_1	p_1	Γ_1
P1	0.4000	0.033	3.001	5.016	1.2	0.0156	1.000	1.2
D1	0.0125	0.786	1.010	0.620	−0.92	0.275	0.575	0.70
D2	0.0125	0.629	0.983	−0.135	–0.053	0.879	1.090	−0.031
D3	0.0125	0.454	0.808	0.353	0.36	0.275	0.575	0.70

TABLE 1. Thermodynamic states for the jump conditions across the incident shock wave (non-dimensional variables).

The above eigenvalues are also used to find the appropriate time step,

$$\Delta t = \min\left(\frac{\sigma\Delta\xi}{\lambda_\xi},\ \frac{\sigma\Delta\eta}{\lambda_\eta}\right), \tag{3.16}$$

where σ is the CFL number.

Since the flow field involves waves moving and interacting in several different directions four permutations of the predictor-corrector sequence are used to eliminate directional bias. Reflective (solid wall) boundary conditions are implemented on the upper, lower, and right-hand boundaries which includes enforcing the tangency condition of the velocity components on the these boundaries in the physical domain. Although cases where the incident shock reflects from the right-hand endwall are computed with no difficulty, incident shocks are not allowed to reach this boundary for the cases shown in this paper.

The shock tube initial conditions used to generate the shock jump conditions in table 1 are from Argrow (1996). With the high-pressure state on the left-hand side of the diaphragm and the low-pressure state on the right-hand side, bursting the diaphragm produces a rightward-propagating compression shock followed by a slower moving contact discontinuity. The resulting Rankine–Hugoniot jump conditions across the shock are then used to restart the calculation. For all cases, the discontinuity is started to the left of the obstacle as shown in figure 2. A complex subsonic inflow boundary condition is avoided by not allowing interior disturbances to reach the left-hand boundary. An expansion shock is similarly started from the jump conditions with the high- and low-pressure states reversed such that the incident shock propagates to the right into the quiescent high-pressure gas. The induced velocity of the gas upon expansion through the shock is to the left in the negative x-direction so that the left-hand boundary in figure 2 becomes an outflow boundary. Table 1 contains the moving incident shock jump conditions for the selected cases.

4. Results

4.1. *Validation of the numerical scheme and gas model*

Argrow & Cox (1993) compare results of the PCTVD scheme to the exact solution of the one-dimensional Riemann problem using the perfect gas state equation. Argrow (1996) shows that the numerical scheme with the van der Waals equation of state approaches the perfect gas solution of the shock tube problem for initial conditions in the dilute gas region.

For the present cases, computation begins with the single rightward-propagating shock located to the left of the obstacle. For all cases, the computations are stopped when the shock reaches $x \approx 0.9$. All cases are run using 300×300 cells with a CFL

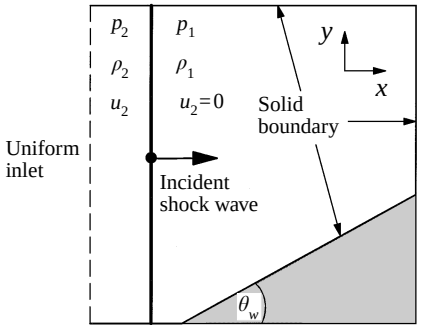

FIGURE 2. Schematic of shock tube domain and initial conditions. The left-hand boundary is set to the post-shock conditions while the obstacle and remaining boundaries are solid.

number range of 0.4–0.7, with the exception of the case shown in figure 7 with the wedge angle of $\theta_w = 60°$ which was run at a CFL number of 0.2.

To investigate the accuracy of the PCTVD simulations, results are compared to the interferogram of Case 7 in Deschambault & Glass (1983) shown in figure 3(*a*). The wave field in figure 3(*a*) is a SMR for argon resulting from a shock Mach number $M_I = 3.20$ incident on a compressive wedge of $\theta_w = 20°$. Figure 3(*b*) shows the isopycnics of the PCTVD scheme starting from these initial conditions using the perfect gas model. Unlike the diagram in figure 2 the incident shock in figure 3(*b*) propagates to the left for a more convenient comparison with the experimental results. The flow field is mapped by superimposing a grey scale with 20 contour lines. Darker shades correspond to higher-density regions while lighter shades correspond to lower-density regions. The contour lines map out densities whose values are equally spaced increments between the highest- and lowest-density values in the flow field. The wave field structure including the Mach stem, triple point, reflected shock, and slipstream are resolved, simulating the experimental results. The density ratios in the labelled regions of the flow field closely agree with the experimental results.

The perfect gas limit of the van der Waals model is validated by running the PCTVD scheme with initial conditions far from the thermodynamic critical point, case P1 in table 1. The resulting isopycnics for an incident Mach number $M_I = 1.65$ and wedge angle of $\theta_w = 20°$ are shown in figure 4(*a*). As expected, the wave field structure for this limiting case of the van der Waals model is that of a SMR, similar to the results that use the perfect gas model shown in figure 3(*b*). Because the incident shock is much weaker for the van der Waals case, the slipstream, though still discernable, is not as obvious as the other structures present in the wave field.

The adequacy of the grid spacing is determined by observing the convergence of the lower-boundary density profiles for the P1 case with increasing grid resolution shown in figure 4(*b*). For each case, the computation is stopped at the same time value. The 300×300 resolution is found to be adequate since the 150×150 resolution results in density differences only of the order of 10^{-3}.

4.2. *Dense gas results*

Initial conditions in the dense gas regime labelled D1–D3 in table 1 are analysed for various obstacle geometries. For the D1 case, $\Gamma > 0$ ahead of the incident compression shock and $\Gamma < 0$ behind it. Figure 5 shows the resulting flow field for a wedge having an angle of $\theta_w = 20°$. The isopycnics of the flow in figure 5(*a*) are depicted in the same manner as in figure 3(*b*). The incident shock is moving to the right at $M_I = 1.23$.

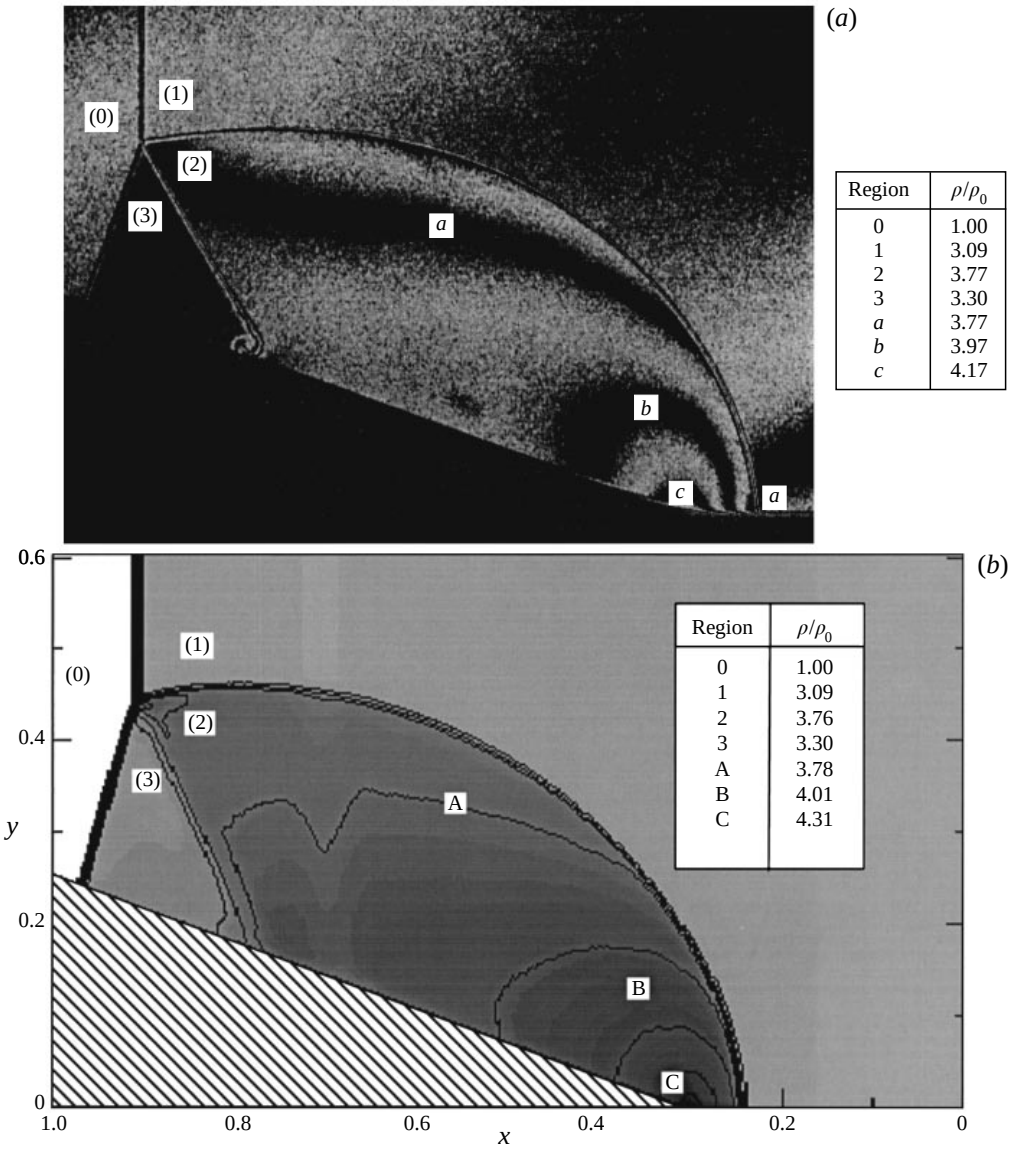

FIGURE 3. SMR for argon. (*a*) Deschambault & Glass's (1983) experimental results for their case 7. $M_I = 3.20$, $\rho_2/\rho_1 = 3.09$, $\theta_w = 20°$. (*b*) Isopycnics PCTVD scheme with the perfect gas model using the initial conditions of case 7.

With the same geometry and conditions using the perfect gas model, a SMR similar to the schematic shown in figure 1(*b*) occurs. This also appears to be the case for the dense gas shock wave. While the reflected shock and Mach stem are resolved, the shock is too weak to clearly present a slipstream in the isopycnic plot. However, the slipstream, though smeared, is evident in the entropy field shown in the enlarged inset of the triple-point region in figure 5(*a*). Differences of the reflection shown in 5(*a*) with a SMR for a perfect gas, like those in figures 3 and 4, include a triple-point that is much closer to the wedge and a reflected shock that remains attached to the front of the wedge. These differences give some indication that certain features such as the

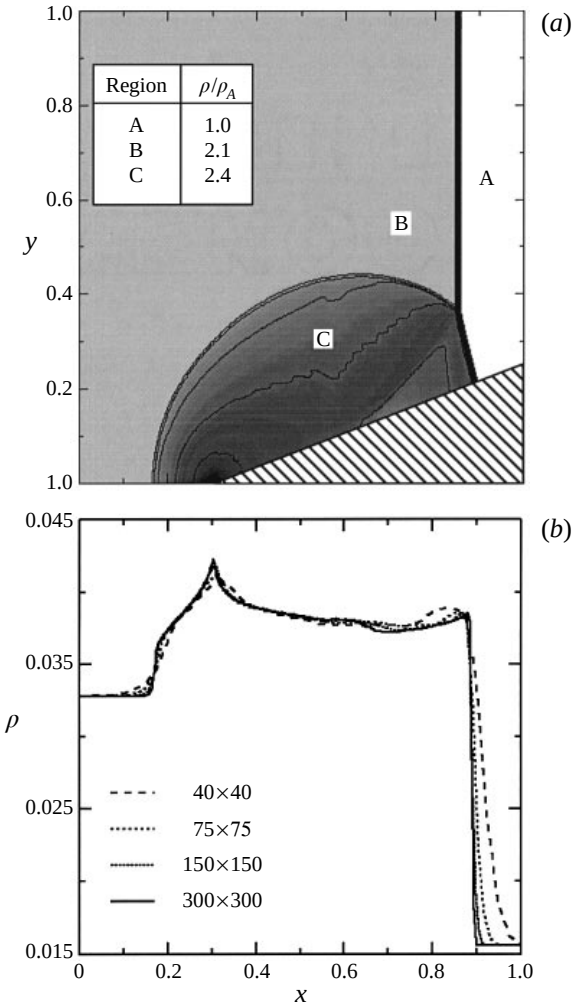

FIGURE 4. Wave field for the P1 case, $\theta_w = 20°$. (*a*) Isopycnics from the PCTVD scheme with the van der Waals model for initial conditions in the perfect gas regime. (*b*) Density ρ profiles along the lower surface for various grid resolutions.

triple point trajectory angle, χ, defined in figure 1(*b*), and the shock detachment angle, i.e. the minimum angle for which the reflected wave will move upstream of the wedge, will be different in a dense gas due to non-classical effects. This is not unexpected since Law & Glass (1971) show that thermodynamic parameters contribute to the triple-point trajectory angle. Also, Cramer (1991*b*) found shock detachment angles for oblique shocks in steady flows of gases with large specific heats to be much higher than those of dilute gases.

The density ρ, Mach number M, and fundamental derivative Γ profiles along the lower surface are shown in figure 5(*b*). Note that M and Γ go through an extremum in the Mach stem at $x \approx 0.9$. Argrow (1996) gives a detailed discussion of why this non-inviscid phenomenon occurs in Euler solutions. The extrema essentially result from the smearing of the shock 'discontinuity' over a finite number of cells. Because the entropy jump $[s]$ across the shock is small ($[s] \leqslant 10^{-1}$ for all cases),

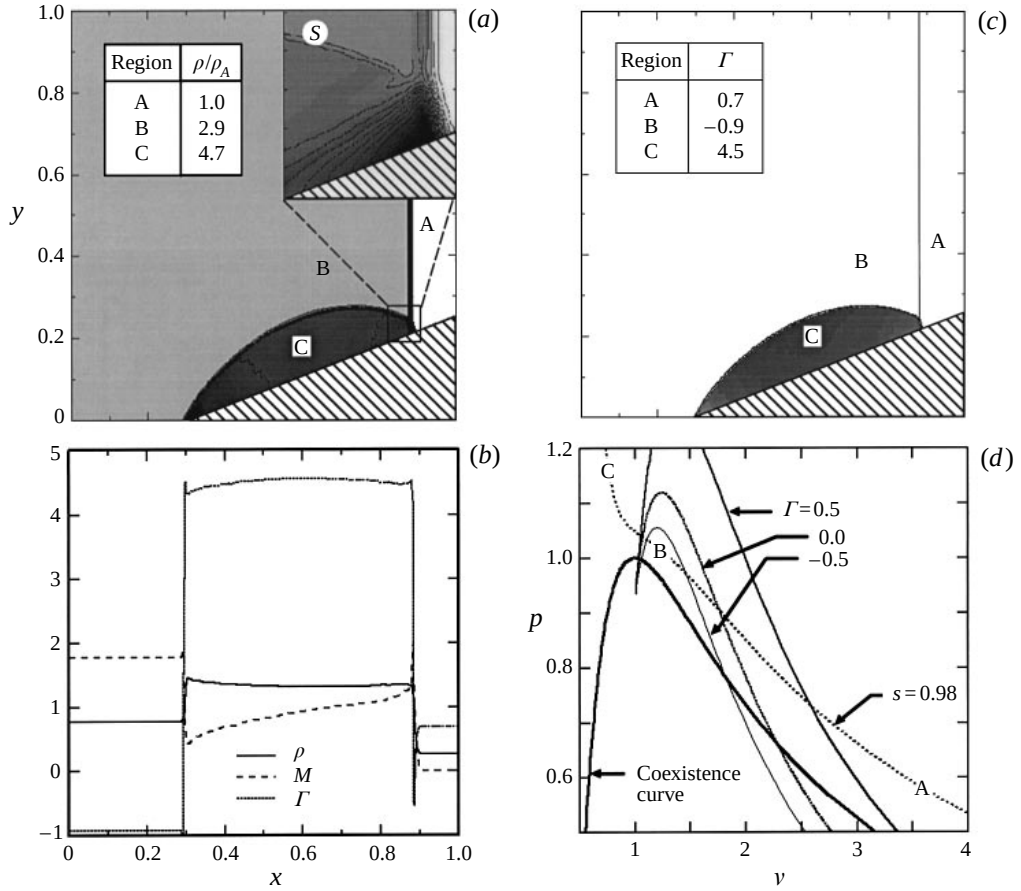

FIGURE 5. Wave field for the D1 case, $\theta_w = 20°$. (*a*) Isopycnics and a magnified inset of the triple-point region showing contours of entropy change, featuring the slipstream. (*b*) Density ρ, Mach number M, and the fundamental derivative Γ profiles on the lower boundary. (*c*) Fundamental derivative, Γ contours. (*d*) A p, v diagram showing the thermodynamic states of the flow field regions along with the coexistence curve, constant-Γ contours, and the isentrope of the initial state of the flow field regions.

the isentropes closely approximate the shock adiabats. This is evident in the p, v diagram in figure 5(*d*) which shows the coexistence curve, constant-Γ contours, and the isentrope of the initial state of the gas upstream of the incident shock, i.e. region A. The thermodynamic conditions of regions B and C in figure 5(*a*) coincide closely with the isentrope $s = 0.98$ of region A. Since the $\Gamma < 0$ region lies between regions A and C, Γ has an extremum through the jump across the Mach stem. The Mach number extremum seems to mimic the viscous structure of weak shocks studied by Cramer (1987), which shows that the Mach number attains an extremum when the local value of Γ changes sign. This is in contrast to the monotone variation of Mach number through perfect gas shocks. Figure 5(*c*) shows the value of Γ in the flow field mapped using a grey-scale as well as the contour lines for $\Gamma = 0$ and $\Gamma = 1$. Darker shades correspond to regions with higher values of Γ.

Flow fields for the D1 case with relatively small and large wedge angles are presented in figures 6 and 7. Isopycnics for the compression shock incident on a

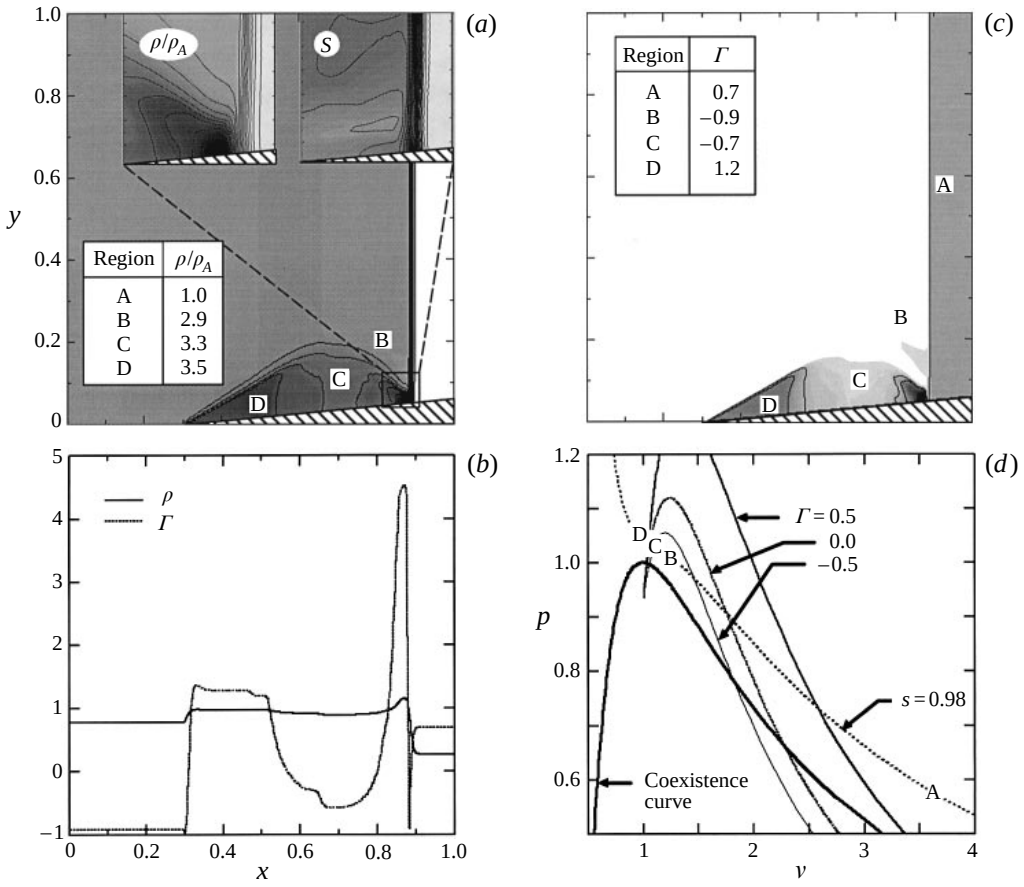

FIGURE 6. Wave field for the D1 case, $\theta_w = 5°$. (*a*) Isopycnics and a magnified inset of the triple-point region showing contours of entropy change. (*b*) Density ρ, and the fundamental derivative Γ profiles on the lower boundary. (*c*) Fundamental derivative Γ contours. (*d*) A p, v diagram showing the thermodynamic states of the flow field regions.

wedge of $\theta_w = 5°$ are shown in figure 6(*a*). Unlike figure 5, the wave field structure is not that of an SMR. The reflected wave lying between regions B and C is a finite compression wave rather than a shock. This is expected since $\Gamma < 0$ in both regions B and C, evident in the Γ contour plot in figure 6(*c*) and the p, v diagram in figure 6(*d*). Although there is a small $\Gamma > 0$ region just behind the incident shock near the wedge surface at $x \approx 0.87$, there is no evidence from this calculation that the reflected compression wave contains a shock in this region. The enlarged density field of this region, which is inset in figure 6(*a*), shows the spreading density contours of a finite compression wave. Also in figure 6(*a*), the inset of entropy contours in the region gives no indication of a slipstream or a triple point such as is found in figure 5(*a*). The form of the reflected wave between regions B and D is difficult to interpret. The density contours in figure 6(*a*) appear to show a shock attached to the front of the wedge that disintegrates into a fan between regions D and C. The location of thermodynamic regions B and D in figure 6(*d*) suggests a fan–shock composite wave as the flow moves through the wave from $\Gamma < 0$ in region B to $\Gamma > 0$ in region D. However, further investigation found no resolvable entropy jump across the wave.

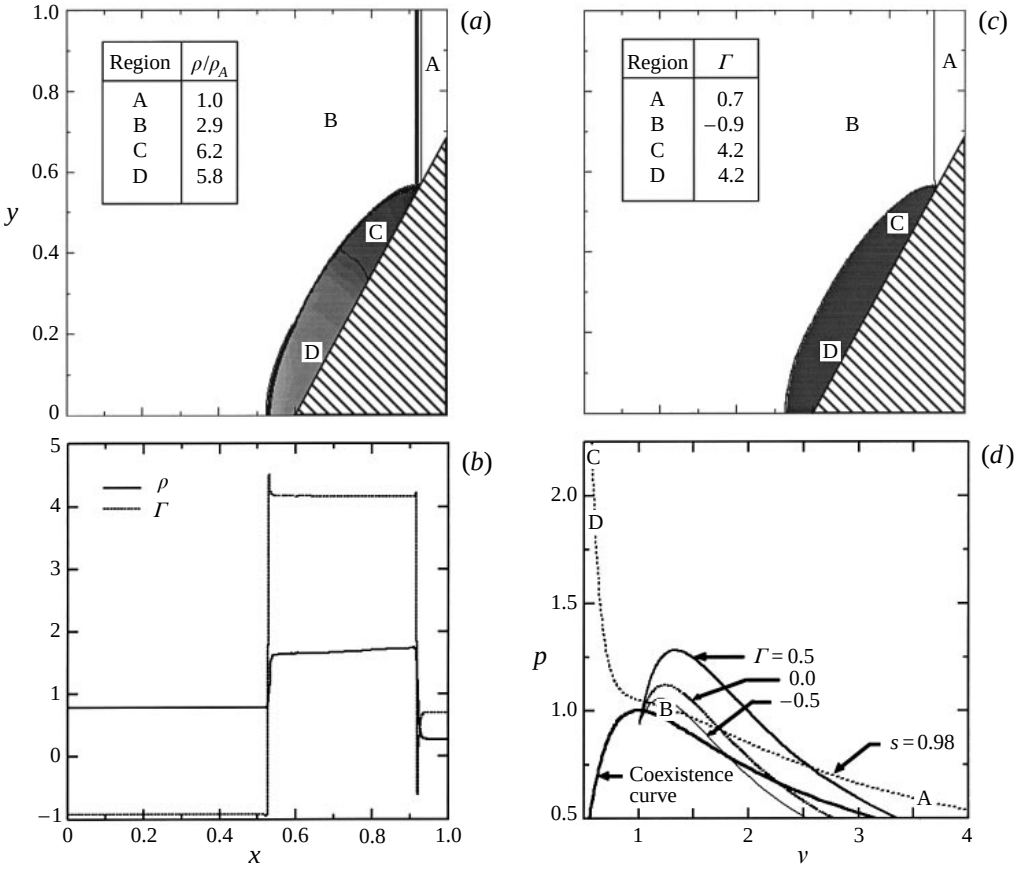

FIGURE 7. As figure 6, but for $\theta_w = 60°$.

This may indicate that the weak reflected shock wave has degenerated completely into a compression fan.

The wave field configuration for the case in figure 6 is somewhat similar to a type of reflection found in perfect gases known as a von Neumann reflection (NR), recently discovered from the numerical computations of Colella & Henderson (1990). The reflected wave of a NR was found to be a self-similar band of finite compression waves that converge into a shock away from the triple point. Similar to the case in figure 6, the NR is found to occur for weak incident shocks and lower wedge angles. Unlike the case in figure 6, the region of the NR in which the reflected wave has finite thickness is very small, too small, in fact, to be resolved experimentally at the time of the study. The compression fan portion of the reflected wave in figure 6 has a much larger scale than the fan found in a NR. This difference is due to the fact that the fan portion of the reflected wave in figure 6 occurs for different physical reasons than that of the NR. The former arises from the thermodynamic condition of $\Gamma < 0$ in the region of the reflected wave for which waves cannot exist as compression shocks, whereas the fan in the NR arises from a fluid dynamic condition for which the three-shock theory fails. Also, while a NR does not have a typical slipstream in the form of a shear discontinuity, still present is a shear layer across which an entropy change occurs. As mentioned earlier, no entropy change is evident in figure 6(*a*) in

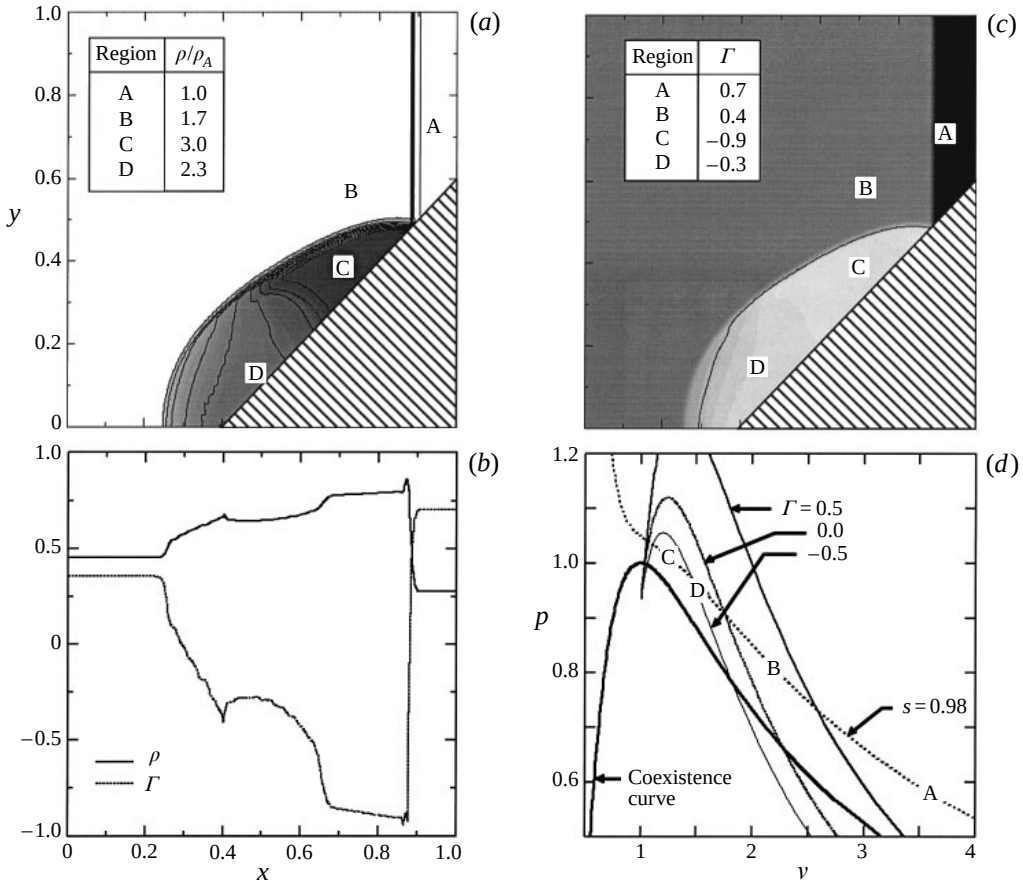

FIGURE 8. As figure 6, but for the D3 case, $\theta_w = 45°$.

this region. In the light of these two differences, the wave configuration in figure 6 does not appear to be a typical NR.

Isopycnics, ρ and Γ profiles along the lower boundary, Γ contours, and the p, v diagram for a wedge angle of $\theta_w = 60°$ for case D1 are shown in figure 7(*a–d*). The reflected wave takes the form of a compression shock under which Γ maintains a fairly constant positive value. This is evident in the p, v diagram in figure 7(*d*) where regions C and D, below the reflected wave in figure 7(*a*), are well above the $\Gamma < 0$ region. Thus, for high wedge angles, the wave field structure for dense gas shocks appears to be consistent with the RR depicted in figure 1(*c*). This is the typical reflection configuration for shocks in perfect gases at high wedge angles such as is shown in the θ, M_I diagram for argon in figure 1(*a*).

Figure 8(*a–d*) shows the flow field starting from the D3 conditions given in table 1 for a wedge angle $\theta_w = 45°$. The incident compression shock is moving to the right at $M_I = 1.18$. For these conditions $\Gamma > 0$ both upstream and downstream of the incident shock. The adiabat connecting these conditions, however, passes through the thermodynamic region of $\Gamma < 0$. The plot of Γ in figure 8(*c*), as well as the p, v diagram in figure 8(*d*), shows that the gas in regions C and D, under the reflected wave shown in figure 8(*a*), have been compressed into the $\Gamma < 0$ region. In the one-dimensional case computed by Argrow (1996), the incident shock with the D3

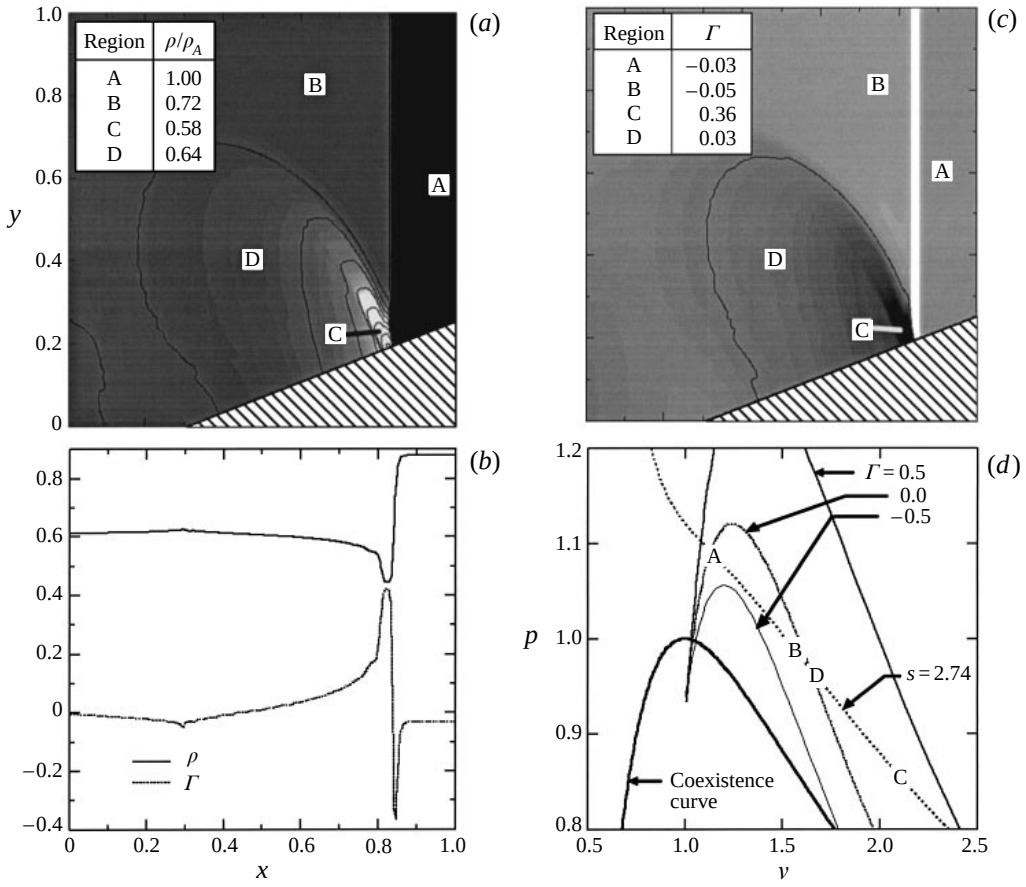

FIGURE 9. As figure 6, but the incipient expansion shock wave field for the D2 case, $\theta_w = 20°$.

conditions reflects from the endwall as a split shock. As explained by Cramer (1989*b*), the shock-splitting phenomenon depends partly on the strength of the shock. For the reflected wave seen in the isopycnics of figure 8(*a*), no split shock is evident since the reflection is not strong enough to compress the gas back into the $\Gamma > 0$ region, i.e. compressed to the extent that region C would lie in the $\Gamma > 0$ region. Although the shock structure shown in the isopycnics of figure 8(*a*) basically resembles a RR, there are differences. The reflected shock separating regions B and C splits into a shock followed by a compression fan between regions B and D and a second compression fan separating regions D and C. This is also evident in the density profile along the lower boundary in figure 8(*b*) where the shock–fan is located at $x \approx 0.3$ and the second fan at $x \approx 0.65$.

The flow field using D2 conditions for an expansion shock with $M_I = 1.05$ incident on a wedge of $\theta_w = 20°$ is shown in figure 9(*a–d*). Here the high-pressure gas is located to the right, upstream of the shock, and the post-shock condition is the low-pressure gas as indicated for this case in table 1. Thus, as the shock propagates to the right, the flow travels to the left after expanding through the shock. Isopycnics of the wave field are shown in figure 9(*a*). The flow immediately behind the incident shock, near the wedge in region C, is expanded to a lower density than the flow behind the incident shock far above the wedge in region B. This left-moving, over-expanded flow

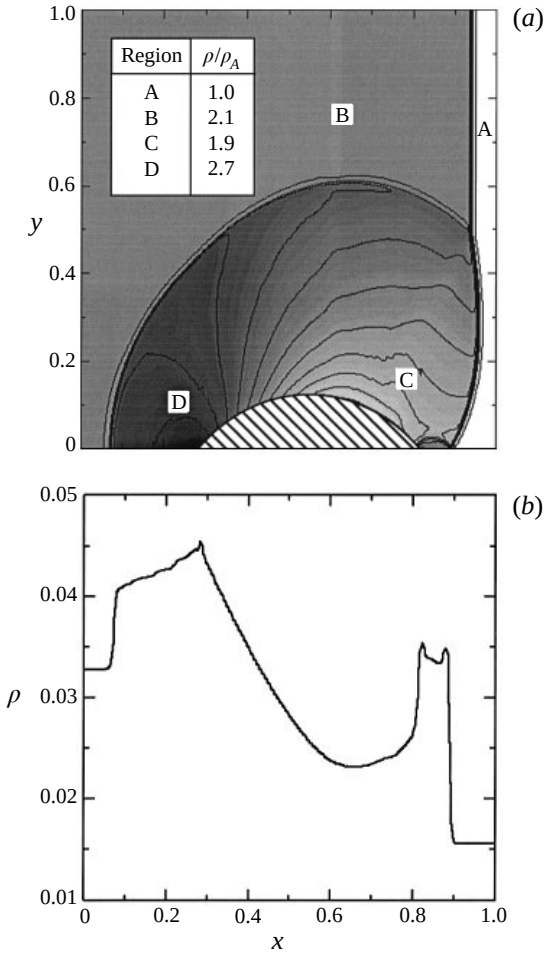

FIGURE 10. Wave field for the P1 case with a circular arc. (*a*) Isopycnics. (*b*) Density ρ on the lower boundary.

is then partially recompressed through what appears to be a weak compression shock extending from the wedge surface near $x = 0.8$. This shock becomes continuously weaker farther above the wedge. The flow is then more gradually compressed as it propagates to the left into region D, as is evident in the density profile on the lower surface shown in figure 9(*b*). As seen in the Γ plot in figure 9(*c*) and the p, v diagram in figure 9(*d*), the fundamental derivative $\Gamma > 0$ in regions C and D to the left of the incident shock, including the region of the compression shock as expected.

A compression shock propagating over a circular arc whose maximum thickness is 12.5% of the total distance between the upper and lower boundaries is shown in figures 10 and 11. The wave field for the P1 conditions with $M_I = 1.65$ is shown in figure 10(*a,b*). The wave field structure of the isopycnics shown in figure 10(*a*) has features similar to both those of Yee (1989), who used a similar numerical scheme for a perfect gas shock over a rounded wedge, and Yang, Lombard & Bershader (1987). The Mach stem has the form of a curved diffracted shock travelling slightly ahead of the incident shock. The triple point, reflected shock, and low-density region on the right-hand side of the arc are also well resolved. In addition, the formation of a

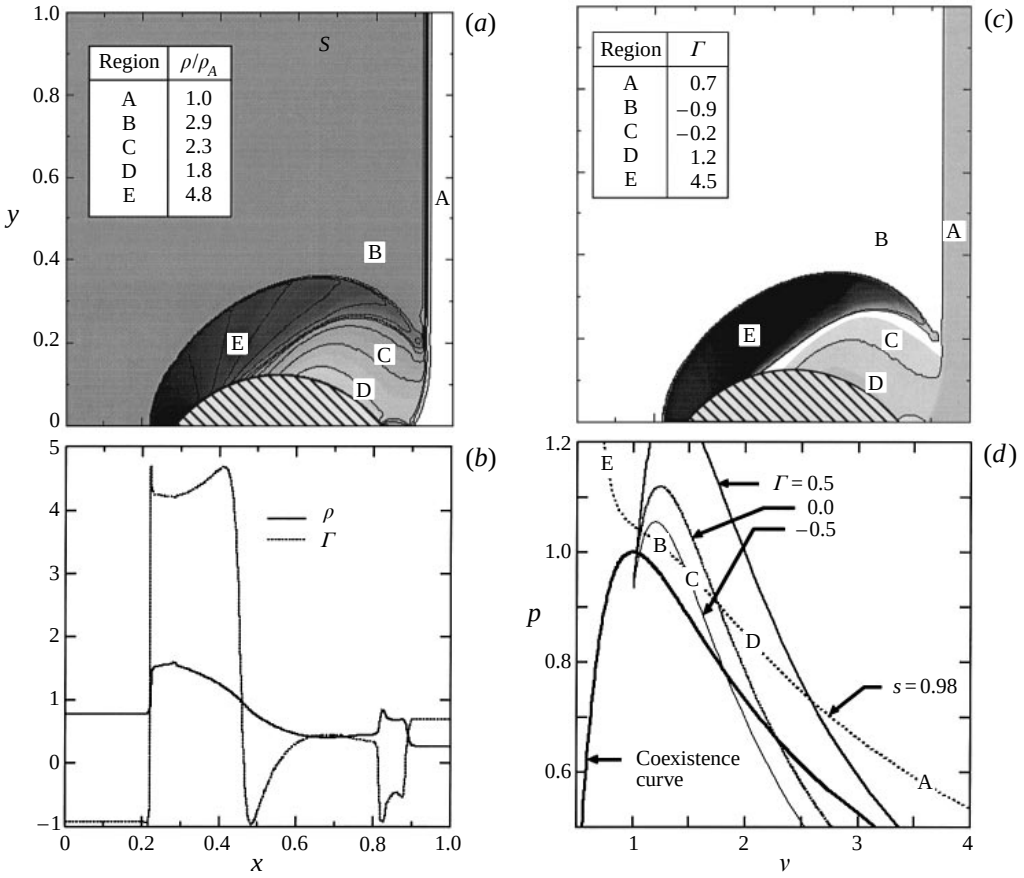

FIGURE 11. Wave field for the D1 case with a circular arc. (*a*) Isopycnics. (*b*) Density ρ and fundamental derivative Γ profiles for the lower boundary. (*c*) Fundamental derivative Γ contours. (*d*) A p, v diagram showing the thermodynamic states of the flow field regions.

secondary compression shock at the right-hand terminus of the arc is fairly evident in figure 10(*a*) and clearly apparent in the density profile for the lower boundary in figure 10(*b*).

The flow field for a compression shock propagating over a circular arc identical to that of figure 10 using the D1 conditions with $M_I = 1.23$ is presented in figure 11(*a–d*). The isopycnics in figure 11(*a*) show that the dense gas flow field lacks a clearly resolved triple point and that the Mach stem does not travel noticeably ahead of the incident shock. The reflected compression shock between regions B and E disintegrates into a compression fan behind the incident shock between regions B and C. Another interesting feature is the formation of an expansion shock above the arc between regions E and C. Note from figure 11(*b*) that on the arc surface this expansion wave is present in the form of a fan and coalesces into a shock above the arc in the $\Gamma < 0$ region. Cramer (1991*a*) illustrates a similar phenomenon of an expansion shock forming above a single airfoil in a steady flow. Both phenomena are consistent with the theory of Thompson (1971) for expansion shock formation where Mach lines predictably converge with decreasing pressure where $\Gamma < 0$. Figure 11(*c*) shows the Γ contours for the wave field, and figure 11(*d*) shows the thermodynamic conditions of the labelled regions. Also interesting to note in figure 11(*a*) is the compression

shock around the right-hand terminus of the arc. Here, the gas is recompressed into the $\Gamma < 0$ region evident in the Γ profile for the lower boundary in figure 11(*b*).

5. Discussion

As anticipated, the wave structures for shock reflections in the dense gas regime are found to be significantly different than those of perfect gas flows over similar geometries. For example, unlike shocks in the perfect gas regime, compression shocks incident on a wedge whose post-shock condition lies in a region of $\Gamma < 0$ apparently cannot form a typical SMR at very low wedge angles such as the $\theta_w = 5^\circ$ case shown in figure 6. The moderate wedge angle ($\theta_w = 20^\circ$) for the case shown in figure 5 results in a SMR, and the high wedge angle ($\theta_w = 60^\circ$) in figure 7 results in an RR. However, features such as triple-point trajectory angles and detachment angles are expected to differ from those of perfect gases due to the thermodynamic properties in the dense gas regime. The structure of many dense gas wave fields are non-intuitive from a classical gas dynamics point of view, e.g. the partial disintegration of the reflected shock into a fan for the D3 case in figure 8 and the weak compression shock behind the expansion shock for the D2 case in figure 9. This is because the fundamental derivative Γ is sensitive to wave and boundary interactions in the thermodynamic region near the critical point. Wave structures are consistent with the inviscid theory with regard to the sign of the fundamental derivative, i.e. compression shocks spread into fans in regions of $\Gamma < 0$, etc. Dense gas flows involving more complex geometries such as the circular arc also show a wealth of non-classical phenomena. For the D1 case shown in figure 11(*a*), the existence of a triple point is not apparent and an expansion shock forms above the arc.

Thus far there has been no attempt to analytically treat shock reflections in the dense gas regime. Although analytical investigation is not the focus of this paper, a brief discussion on the challenges of such an investigation is warranted. Analytical approaches for the RR and SMR configurations are developed by von Neumann (1943) through the 'two-shock theory' and 'three-shock theory', respectively. Two difficulties arise when trying to approach a solution with these theories using a gas model that accounts for real gas effects, such as the van der Waals model: (i) the complexity of the state equations, and (ii) the validity of the physical models behind these theories for dense gas flows. Regarding (i), the two-shock theory for a RR consists of nine equations and 13 parameters for a gas assumed to be thermally perfect and in thermodynamic equilibrium. Using the perfect gas state equation reduces the problem to a single sixth-order polynomial for which four roots can be discarded leaving the weak and strong shock solutions (Henderson 1982). Referring to (2.1) and (2.2), the van der Waals model is more complex since the gas is thermally imperfect as well as calorically imperfect, i.e. $e = e(\rho, T)$. The simplifications of shock reflections in perfect gases are clearly lost when modelling dense gases using even the simplest non-ideal gas model. For example, as mentioned in §1, reflection categories for perfect gases with a constant $\gamma = c_p/c_v$ are found to be a function of θ_w and M_I only. For perfect gases the speed of the incident shock is a function of γ and the pressure ratio across the shock, i.e. $M_I = M_I(\gamma, p_2/p_1)$. For dense gases, however, the actual values of the pressures across the shock become important in determining the proximity of the thermodynamic states to the $\Gamma < 0$ region.

Regarding (ii), the three-shock theory will break down for weak incident waves, which indicates that the physical model for weak reflections is incorrect (Colella & Henderson 1990). As stated previously, shock waves in the dense gas regime are

generally weak ($M_I \leqslant 1.23$ for the cases presented here). In addition, reflections in the dense gas regime can potentially consist of composite waves, e.g. a shock–fan combination, which are not readily treatable through analytical approaches of the two-shock and three-shock theories.

The objective of the present paper is to present results of recent numerical experiments that predict non-classical phenomena for flows of dense gases. Noted earlier is that very little experimental data are available for dense gas flows that display the phenomena of interest in the present paper. The existing data are either not applicable to the present cases (e.g. the two-phase results of Thompson *et al.* 1986), or the original interpretation of the results is questionable (Borisov *et al.* 1983). The simulations of the present paper predict what we expect to see experimentally. As noted, the only pertinent experimental data presently available are for a perfect gas. PCTVD results with the perfect gas model accurately reproduce the experimental data of Deschambault & Glass (1983) as shown earlier.

In spite of the lack of experimental evidence at this time, advanced computational methods provide powerful tools for the design and analysis of complex physical systems such as dense gas flows. Although simulations cannot replace carefully planned experiments, they complement experiments in a number of ways. In the past numerical results were often compared to existing experimental databases for validation and to build confidence in their ability to simulate physical systems. The maturation of computational fluid dynamics (CFD) over the past 30 years is exemplified by the ability of state-of-the-art shock capturing methods, such as the PCTVD scheme in the present paper, to accurately model Euler flows over simple geometries.

At present, simulations often precede experimental evidence of phenomena. For instance, it is commonplace in particle physics for the existence of subatomic particles to be predicted before experimental verification. In fact, the numerical predictions allow experimenters to focus their attention on certain predicted phenomena to verify a particle's existence. Our approach is similar in that the calculations presented here provide guidance for experiments. Owing to the small, finite range of thermodynamic conditions in which dense gas phenomena can be observed, experiments are difficult to design and perform. Numerical simulations, such as shown in this paper, will simplify the task. Another important application of CFD is the 'virtual measurement' of variable and parameter combinations that are very difficult or even impossible to obtain experimentally, thus providing insight into physical processes that may exceed what can be accomplished with current experimental techniques.

6. Summary and conclusions

Two-dimensional unsteady wave fields for an inviscid van der Waals gas near the thermodynamic critical point are examined for selected cases. To the authors' knowledge, this is the first numerical analysis of physically realistic time-accurate unsteady single-phase flow of dense gases over obstacles. Significant differences in wave field structures between dense gases and perfect gases are clearly demonstrated. Certain non-classical phenomena observed in these cases, such as the total or partial disintegration of compression shocks, may prove to be useful in certain engineering applications, e.g. flow through a turbine cascade. The van der Waals equation of state and constant-c_v assumption are used more for simplicity than accuracy. An equation of state which is more accurate near the thermodynamic critical point will improve the numerical simulations at the expense of algorithm complexity and computation time.

A thorough study of wave reflections in the dense gas regime is of great importance if the technological potential of dense gases in the engineering sciences is to be completely realized. Therefore, future work will include more sophisticated numerical schemes and gas models to simulate flows over a wider range of geometries for both steady and unsteady cases. In addition, there is a need for experiments to provide more data for validation of the simulations, e.g. shock tube experiments for working fluids commonly used in organic Rankine cycles.

The authors acknowledge the National Science Foundation for support of this work through the grant CTS-9614207.

REFERENCES

Aldo, A. C. & Argrow, B. M. 1995 Dense gas flow in minimum length nozzles. *Trans. ASME: J. Fluids Engng* **117**, 270–276.

Anders, J. B. 1993 *Heavy gas wind-tunnel research at Langley Research Center. ASME Paper* 93-FE-5.

Anderson, W. K. 1991 Numerical study on using sulfur hexafluorideas a test gas in wind tunnels. *AIAA J.* **29**, 23–51.

Argrow, B. M. 1996 Shock tube flow for dense gases. *Shock Waves* **6**, 241–248.

Argrow, B. M. & Cox, R. A. 1993 A Quantative, Second-Law Base Measure of Accuracy of Numerical Schemes. *AES* Vol. 30/*HTD* Vol. 266, pp. 359–384.

Ben-Dor, G. 1992 *Shock Wave Reflection Phenomena.* Springer.

Bethe, H. A. 1942 The theory of shock waves for an arbitrary equation of state. *Office Sci. Res. & Dev. Rep.* 545.

Borisov, A. A., Borisov, Al. A., Kutateladze, S. S. & Nakoryakov, V. E. 1983 Rarefaction shock wave near the critical liquid-vapour point. *J. Fluid Mech.* **126**, 59–73.

Causon, D. M. 1988 A total variation diminishing scheme for computational aerodynamics. In *Numerical Methods for Fluid Dynamics III,* pp. 449–457. Clarendon.

Colella, P. & Henderson, L. F. 1990 The von Neumann paradox for the diffraction of weak shock waves. *J. Fluid Mech.* **213**, 71–94.

Cramer, M. S. 1987 Structure of weak shocks in fluids having embedded regions on negative nonlinearity. *Phys. Fluids* **30**, 3034–3044.

Cramer, M. S. 1989*a* Negative nonlinearity in selected fluorocarbons. *Phys. Fluids* A **1**, 3034–3044.

Cramer, M. S. 1989*b* Shock splitting in single-phase gases. *J. Fluid Mech.* **199**, 281–296.

Cramer, M. S. 1991*a* Nonclassical dynamics of classical gases. In *Nonlinear Waves in Real Fluids*, pp. 91–145 Springer.

Cramer, M. S. 1991*b* On the Mach number variation in steady flows of dense hydrocarbons. *Trans. ASME: J. Fluids Engng* **113**, 675–680.

Cramer, M. S. & Best, L. M. 1991 Steady, isentropic flows of dense gases. *Phys. Fluids* A **3**, 219–226.

Cramer, M. S. & Kluwick, A. 1984 On the propagation of waves exhibiting both positive and negative nonlinearity. *J. Fluid Mech.* **142**, 9–37.

Cramer, M. S. & Sen, R. 1986 Shock formation in fluids having embedded regions of negative nonlinearity. *Phys. Fluids* **29**, 2181–2191.

Curran, H. M. 1981 Use of Organic Working Fluids in Rankine Engines. *J. Energy* **5**(4), 218–223.

Davis, S. F. 1987 A simplified TVD finite difference scheme via artificial viscosity. *SIAM J. Sci. Statist. Comput.* **8**, 1–18.

Deschambault, R. L. & Glass, I. I. 1983 An update on non-stationary oblique shock-wave reflections: actual isopycnics and numerical experiments. *J. Fluid Mech.* **131**, 27–57.

Emanuel, G. 1987 *Advanced Classsical Thermodynamics.* AIAA Education Series, New York.

Henderson, L. F. 1982 Exact expressions for shock reflexion transition criteria in a perfect gas. *Z. Angew. Math. Mech.* **62**, 258–261.

Kluwick, A. 1993 Transonic nozzle flow of dense gases. *J. Fluid Mech.* **217**, 661–688.

LAMBRAKIS, K. C. & THOMPSON, P. A. 1972 Existence of real fluids with a negative fundamental derivative Γ. *Phys. Fluids* **15**, 933–935.

LAW, C. K. & GLASS, I. I. 1971 Diffraction of strong shock waves by a sharp compressive corner. *CASI Trans.* **4**, 2–12.

NEUMANN, J. VON 1943 Oblique reflection of shocks. *Explosives Res. Rep.* 12, Navy Dept., Bureau of Ordinance, Washington, DC, US Dept Comm. Off. Tech. Serv. No. PB37079.

SCHNERR, G. H. & LEIDNER, P. 1991 Diabatic supersonic flows of dense gases. *Phys. Fluids* A **3**, 2445–2458.

SCHNERR, G. H. & LEIDNER, P. 1993*a* Two-dimensional nozzle flow of dense gases. *Fluids Engineering Conf. Washington DC*.

SCHNERR, G. H. & LEIDNER, P. 1993*b* Numerical investigation of axial cascades for dense gases. *Pacific International Conf. on Aerospace Science and Technology, Taiwan, Republic of China.*

THOMPSON, P. A. 1971 A fundamental derivative in gas dynamics. *Phys. Fluids* **14**, 1843.

THOMPSON, P. A., CAROFANO, G. C. & KIM, Y. 1986 Shock waves and phase changes in a large-heat-capacity fluid emerging from a tube. *J. Fluid Mech.* **166**, 57–92.

THOMPSON, P. A. & LAMBRAKIS, K. C. 1973 Negative shock waves. *J. Fluid Mech.* **60**, 187–208.

YANG, J. Y., LOMBARD, C. K. & BERSHADER, D. 1987 Numerical simulation of transient inviscid shock tube flows. *AIAA J.* **25**, 245–251.

YEE, H. C. 1989 A class of high-resolution explicit and implicit shock capturing methods. *NASA TM* 101088.

ZEL'DOVICH, YA. B. 1946 On the possibility of rarefaction shock waves. *Zh. Eksp. Teor. Fiz.* **4**, 363–364.